Green Chemistry

PAPER

View Article Online
View Journal | View Issue

Cite this: *Green Chem.*, 2024, **26**, 6089

Exploring hybrid hard carbon/Bi_2S_3-based negative electrodes for Na-ion batteries†

Blaž Tratnik, [a] Sergio Aina, [c,d] Elena Tchernychova,[a] Matej Gabrijelčič,[a,e] Gregor Mali, [a] Maria Pilar Lobera,[c,d,f] Maria Bernechea, [c,d,f,g] Mathieu Morcrette, [h,i,j] Alen Vizintin *[a] and Robert Dominko [a,b,j]

The study presents a hybrid hard-carbon/nanocrystalline-Bi_2S_3 material applicable for negative electrodes in sodium-ion batteries. Through a series of comprehensive analyzes, including electrochemical measurements, *operando* XRD, *ex situ* solid-state NMR, and high-resolution STEM imaging, the effectiveness of the HC/Bi_2S_3 hybrid configuration in the negative electrode function is elucidated with a focus on the underlying charge storage mechanism. Electrochemical analysis demonstrates the improved performance of the hybrid materials over the pristine HC negative electrode and highlights the robustness and stability of the HC/Bi_2S_3 hybrids over prolonged cycling even under high current densities. Here, the final capacities observed after 100 cycles reached a value of 252 mA h g^{-1}, compared to 216 mA h g^{-1} of pristine HC. Cyclic voltammetry measurements demonstrate a complex charge storage behavior that integrates both surface and diffusion-driven processes at different potentials during reduction and oxidation. A series of phase transformations during cycling observed in *operando* XRD expose irreversible reactions during the initial cycle between Bi_2S_3 and sodium ions, such as the breakdown of the Bi_2S_3 nanocrystal structure. This phenomenon is further confirmed by the detection of Na_2S species using *ex situ* solid-state NMR. High-resolution STEM imaging reveals morphological changes in Bi_2S_3 nanocrystals and highlights their resistance to pulverization due to their nanoscale dimensions. This work provides comprehensive insights into the electrochemical performance of the HC/Bi_2S_3 and sheds light on specific mechanisms and reactions occurring during cycling.

Received 31st January 2024,
Accepted 15th April 2024

DOI: 10.1039/d4gc00564c

rsc.li/greenchem

1. Introduction

As global energy consumption continues to rise, the focus is now shifting from fossil fuels to renewable energy sources to address resource depletion, environmental pollution, and rising energy costs.[1] Integrating renewable energy sources into the power grid necessitates efficient energy storage systems. While Li-ion batteries (LIBs) continue to dominate the market for electric transportation and portable electronics, Na-ion batteries (SIBs) have emerged as a top contender for stationary energy storage systems in conjunction with renewable energy sources, due to the abundance of sodium.[2,3]

Hard carbons (HCs) have proven to be the most feasible choice for negative electrodes and are currently utilized in most standard SIB configurations.[4] The reason for their widespread use is their cost-effectiveness, high storage capacity, and the possibility of sourcing them from waste biomass.[5–7] However, most HCs have limited capacities, typically ranging between 280 mA h g^{-1} and 320 mA h g^{-1}, as highlighted in various studies.[8–13] Therefore, continuous efforts aim to further enhance their performance through diverse modification strategies, such as heteroatom doping,[14–16] altering

[a]National Institute of Chemistry, Hajdrihova 19, 1000 Ljubljana, Slovenia. E-mail: alen.vizintin@ki.si
[b]Faculty of Chemistry and Chemical Technology, University of Ljubljana, Večna pot 113, 1000 Ljubljana, Slovenia
[c]Instituto de Nanociencia y Materiales de Aragón (INMA), CSIC-Universidad de Zaragoza, Zaragoza, 50009, Spain
[d]Department of Chemical and Environmental Engineering (IQTMA), University of Zaragoza, 50018 Zaragoza, Spain
[e]Faculty of Mathematics and Physics, University of Ljubljana, Jadranska 19, 1000 Ljubljana, Slovenia
[f]Centro de Investigación Biomédica en Red de Bioingeniería, Biomateriales y Nanomedicina, Instituto de Salud Carlos III, 50018 Zaragoza, Spain
[g]ARAID, Government of Aragón, 50018 Zaragoza, Spain
[h]Laboratoire de Réactivité et Chimie des Solides (LRCS), UMR CNRS 7314, Université de Picardie Jules Verne, Hub de l'Energie, 15 rue Baudelocque, 80039 Amiens Cedex, France
[i]Réseau sur le Stockage Electrochimique de l'Energie RS2E, FR CNRS 3459, Hub de l'Energie, Amiens, France
[j]ALISTORE-European Research Institute, CNRS FR 3104, Hub de l'Energie, Rue Baudelocque, 80039 Amiens Cedex, France

† Electronic supplementary information (ESI) available. See DOI: https://doi.org/10.1039/d4gc00564c

carbon morphology *via* templating[17,18] and synthesis of nanostructured hybrid carbon-metal composites.[19–21]

The incorporation of nanostructured metal oxides or chalcogenides into a highly conductive carbon matrix, such as HC, enhances charge-storage capabilities by leveraging the high capacities of metallic compounds, while the conductive properties of carbon improve cycling performance and rate capabilities.[22–24] Metal chalcogenides, in particular, have drawn considerable attention as anode materials for SIBs owing to their elevated reversible capacities compared to metal oxides.[25,26] Typically, two distinct reaction mechanisms are observed for metal chalcogenides. On one hand, chalcogenide compounds containing Fe, Co, and Ni metals, which become electrochemically inactive in this structural configuration, undergo an initial intercalation into a layered structure, followed by a reversible conversion of sulfide/selenide species. On the other hand, chalcogenide compounds containing Sn, Sb, and Bi metals in their electrochemically active form follow a similar intercalation step but further engage in synergistic conversion and alloying reactions. This distinctive behavior endows these metals with enhanced electrochemical properties compared to their inactive counterparts.[27]

Among the metal chalcogenide compounds, bismuth chalcogenides, Bi_2X_3 (X = S, Se), are interesting candidates for hybrid carbon-metal composites owing to their anisotropic layered structure which could allow for sodium accommodation,[28] high volumetric capacity (4200–4500 mA h cm^{-3}),[29,30] redox reaction with sodium,[31] and easy and tunable synthesis.[32] Bi_2S_3 is of particular interest due to its higher gravimetric capacity, *e.g.* 625 mA h g^{-1} for Bi_2S_3, compared to 491 mA h g^{-1} for Bi_2Se_3.[33] Despite the similarities in Li and Na chemistry in rechargeable batteries, the larger size of sodium ions leads to considerable volume expansion in the Bi_2S_3 structure.[31] Consequently, the mechanistic studies of Bi_2S_3 for sodium storage are much more limited. Complicating matters further, the existing literature provides conflicting results. Sun *et al.*[34] focused on microsized Bi_2S_3 anodes whereas Li *et al.*[35] examined submicrometer Bi_2S_3 particles coated with graphite. Both studies suggest a two-stage sodium charge storage mechanism involving initial conversion to Na_2S followed by sodium intercalation into the bismuth structure. In contrast, Sottmann *et al.*[36] exploring a nanosized Bi_2S_3 anode and Yang *et al.*[37] investigating Bi_2S_3 nanocrystal-modified carbon nanotubes propose a different two-stage charge storage mechanism consisting of conversion to Na_2S in the initial stage of the process, followed by alloying of sodium with bismuth rather than simple intercalation.

In the frame of this work, we aimed to (i) improve the electrochemical performance of HC by the addition of nanostructured Bi_2S_3 and (ii) clarify the Bi_2S_3 nanocrystal sodium storage mechanism discrepancies shown in the state-of-the-art literature. To our knowledge, there are no reports describing such HC hybridization for SIBs. Different hybrid HC/Bi_2S_3 materials with various mass loadings of Bi_2S_3 nanocrystals were prepared with the addition of 3-mercaptopropionic acid (MPA) acting as a bonding-enhancing agent. The kinetic limiting processes during cycling were addressed using cyclic voltammetry (CV) measurements. Through *operando* X-ray diffraction (XRD) and *ex situ* solid-state nuclear magnetic resonance (ssNMR) measurements, we were able to identify several phase transformations during the sodiation and desodiation processes. *Post-mortem* TEM investigations of pristine and cycled electrodes shed light on the nature of hybrid HC/Bi_2S_3 material volume expansion. Based on the findings, we propose a sodium charge storage mechanism within HC/Bi_2S_3 hybrids.

2. Results and discussion

To investigate the influence of Bi_2S_3 content on the performance of SIBs, two sets of hybrid negative electrodes were prepared and denoted as C1400 °C + MPA + 5 wt% Bi_2S_3 (HC-MPA/5BS) and C1400 °C + MPA + 10 wt% Bi_2S_3 (HC-MPA/10BS). Additionally, two sets of hybrid negative electrodes without MPA linker were prepared and tested as a reference. These were denoted as C1400 °C + 5 wt% Bi_2S_3 (HC/5BS) and C1400 °C + 10 wt% Bi_2S_3 (HC/10BS) (see Note 1 in ESI†). The impact of the MPA linker was demonstrated using XPS analysis of Bi 4*f* high-resolution spectra. Here, the values of Bi–O/Bi–S ratio (0.4 *vs.* 2.2 for HC/BS, see Fig. S1 and Note 1 in ESI†) as well as examination of Bi $4f_{5/2}$ and Bi $4f_{7/2}$ fitted components suggest that MPA acts as a linker between the carbon and Bi_2S_3 nanocrystals leading to a more stable bonding in the HC-MPA/BS based substrate.

Both mass loadings of Bi_2S_3 on HC-MPA were examined by XRD to assess the presence and crystal structure of Bi_2S_3 nanocrystals. The XRD patterns are consistent with the reference pattern for Bi_2S_3 (ICDD: 00-043-1471). This confirms the presence of the Bi_2S_3 nanocrystals (Fig. 1a) along with the prominent (002) and (100) carbon peaks. To verify whether the mass loadings of Bi_2S_3 nanocrystals on the HC-MPA substrate are in accordance with the synthesis procedure, the TG analysis (Fig. 1b) was performed under airflow. The materials exhibit several stages of mass loss during the measurement. The initial loss is observed at approximately 230 °C, corresponding to the decomposition of the MPA linker. The HC-MPA substrate undergoes the second and final mass loss between 500 °C and 700 °C. Due to the oxidative atmosphere, the loss is attributed to the burning process of the organic material, in this case, hard carbon.[38,39] For hybrid HC-MPA/BS materials, the TG curve above 450 °C is split into two contributions. The detected mass loss at 550 °C is ascribed to the oxidation process of the sulfide species, leading to the release of SO_2.[40] Following the oxidation, the final obtained product is Bi_2O_3.[40] The nanocrystal mass loadings determined from the TG measurements are 5.5 wt% and 11 wt% for HC-MPA/5BS and HC-MPA/10BS, respectively.

The electrochemical performance of the hybrid HC-MPA/BS materials was studied in a SIB half-cell configuration. Fig. 2a shows the fifth cycle at a current density of C/10 of HC, HC-MPA/5BS and HC-MPA/10BS. In the sodiation and desodiation curves, two small plateaus can be identified in the high

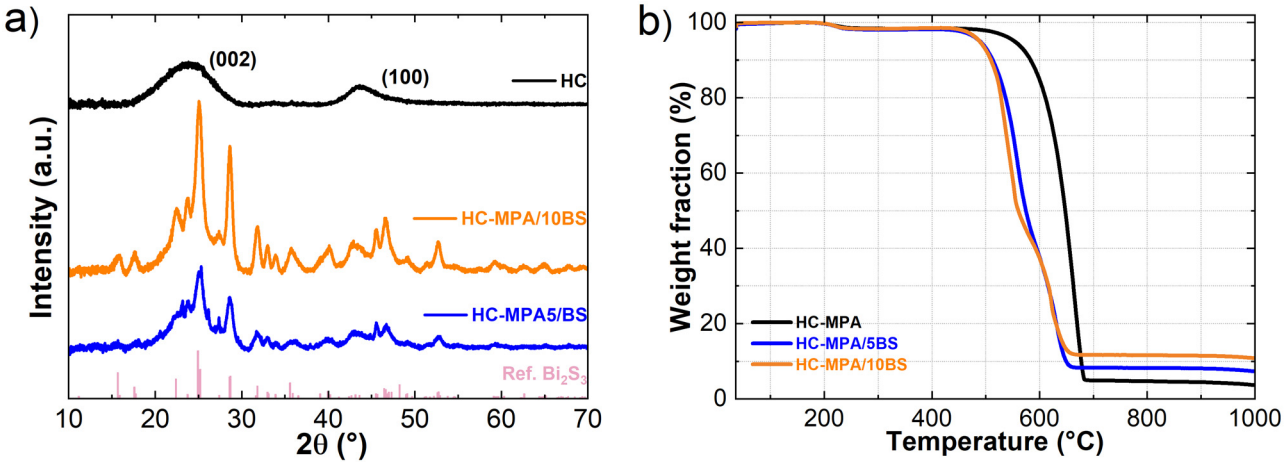

Fig. 1 (a) XRD patterns of HC-MPA/BS (Bi_2S_3 reference is added for comparison – ICDD: 00-043-1471), and (b) TG analysis of HC-MPA/BS.

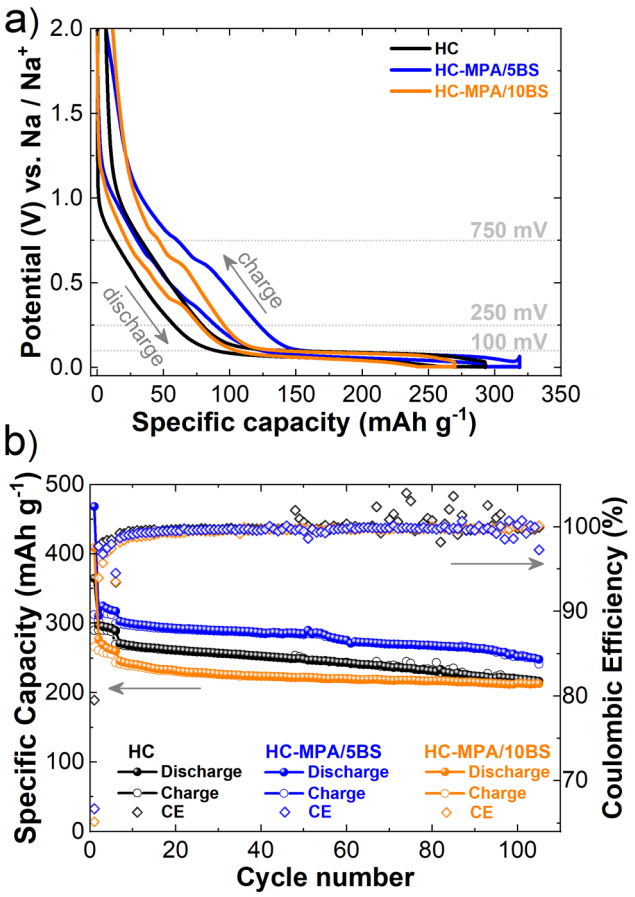

Fig. 2 (a) Electrochemical curves of the fifth formation cycle, and (b) prolonged cycling of HC-MPA/BS. Charge/discharge capacities are presented on the left *Y*-axis and coulombic efficiency is presented on the right *Y*-axis. Five formation cycles were performed with the current rate of C/10 followed by 100 cycles at 1C. A constant voltage step was applied at the lower cut-off of 5 mV.

voltage region between 750 and 250 mV. These plateaus correspond to the phase reaction of sodium with Bi_2S_3 nanocrystals and are more prominent in the case of HC-MPA/10BS material. In the low voltage region below 100 mV, another longer plateau is observed, resembling the sodium intercalation and pore-filling process in HC.[41] The capacity contributions obtained from the sloping and plateau regions are strongly dependent on the addition of Bi_2S_3 nanocrystals (Fig. S2†). The relative contribution of the sloping region increases with the increasing Bi_2S_3 loading, from 31% for HC to 39% for HC-MPA/5BS, and finally to 41% for HC-MPA/10BS. However, in terms of absolute sloping capacity, the highest capacity is provided by HC-MPA/5BS material (Fig. S2†). The decreasing relative contribution from a longer plateau region below 100 mV at the same time demonstrates that the addition of Bi_2S_3 nanocrystals affects both the sodium's intercalation into HC and the consequent pore-filling process. The initial discharge capacities measured at a current density of C/10 (Fig. 2b) are 468 mA h g^{-1} and 410 mA h g^{-1} for HC-MPA/5BS and HC-MPA/10BS, respectively, while the initial coulombic efficiency (ICE) amounts to 67% and 65% for HC-MPA/5BS and HC-MPA/10BS, respectively, compared to 80% for HC. Literature reports indicate Bi_2S_3 nanocrystals exhibit low ICEs,[31,39,42] therefore, it is not surprising an ICE decrease is observed for both HC-MPA/BS materials, compared to pristine HC. After the initial formation cycles, the coulombic efficiency stabilizes, reaching values above 99% (Fig. 2b). Fluctuations in coulombic efficiency are observed for HC throughout 100 cycles, with minor variations also occurring for HC-MPA/5BS in the last five cycles. Meanwhile, HC-MPA/10BS presents very stable cycling. With the increase of current density to 1C after the five formation cycles, a slight stability improvement is observed for HC-MPA/BS with capacity retention values reaching 75%, 78%, and 82% for HC, HC-MPA/5BS, and HC-MPA/10BS, respectively (Fig. 2b). The final capacities after 100 cycles were 216 mA h g^{-1}, 252 mA h g^{-1}, and 213 mA h g^{-1} for HC, HC-MPA/5BS, and HC-MPA/10BS, respectively. These results indicate that the addition of 5 wt% Bi_2S_3 increases the sloping region of the galvanostatic curve and delivers a more stable capacity fade, while the addition of 10 wt% Bi_2S_3 has a rather detrimental effect on the hybrid materials' performance.

Further assessment of the electrochemical properties of both pristine and hybrid materials involved rate performance analysis, with the resulting discharge capacities shown in Fig. S3a.† Notably, HC-MPA/5BS and HC-MPA/10BS exhibited high capacities during the initial formation cycle, followed by high irreversibility in the subsequent cycle. After the formation cycles, HC showed a gradual capacity decrease (Fig. S3b†), while HC-MPA/5BS (Fig. S3c†) and HC-MPA/10BS (Fig. S3d†) demonstrated relatively stable cycling at a rate of C/10. However, all materials showed a continuous capacity decay with increasing current density and eventually stabilized at rates of 2C and 5C. Nevertheless, capacities below 50 mA h g^{-1} were recorded at these current densities. Notably, upon reverting to a lower current density of C/10 resulted in significant capacity recovery, reaching 93%, 96%, and 96% of the initial C/10 capacity for HC, HC-MPA/5BS, and HC-MPA/10BS, respectively. The addition of 5 wt% Bi_2S_3 nanocrystals again leads to an increase in capacity for the hybrid material. However, the effect of the Bi_2S_3 nanocrystals addition is less pronounced at higher current densities. It should be noted that constant voltage step at the lower cut-off was not applied during the rate performance test, which explains the lower capacity values compared to those shown in Fig. 2b.

The obtained total capacity can further be divided into different contributions, more specifically, the contributions from the surface-driven processes, such as adsorption and pseudocapacitance, and contributions from the diffusion-limited processes, such as intercalation or pore filling. To assess the origins of these kinetic limiting factors in hybrid HC-MPA/BS, cyclic voltammetry (CV) measurements in a three-electrode cell were performed (Fig. S4†). Firstly, the CVs for all materials have been measured to visualize all present electrochemical processes (Fig. S5†). The current response of HC (Fig. S5a†) shows a reduction and an oxidation peak in the low voltage region, while no peaks in the sloping region could be observed. A similar feature is detected in the HC-MPA (Fig. S5b†) current response, highlighting that the MPA linker is electrochemically inactive. Both HC-MPA/5BS and HC-MPA/10BS (Fig. S5c and d†) show similar additional current responses in the sloping region. Due to higher Bi_2S_3 loading in HC-MPA/10BS (Fig. S5d†), the current response is more pronounced. In both hybrid materials, an irreversible reduction peak is observed at 1.1 V, with the first reversible reduction peak detected at 590 mV, and the second, more pronounced at 390 mV. Both reversible peaks can also be observed during the oxidation phase, but they shift to higher voltages of 640 mV and 780 mV. This phenomenon can be caused by the overpotential and/or kinetic effects due to Bi_2S_3 phase changes (alloying) during cycling. The observed similarities in CV behavior confirm analogous charge storage mechanisms for both Bi_2S_3 loadings.

In addition, the three-electrode measurements were performed at different sweep rates to distinguish between the observed contributing phenomena, *i.e.* whether a particular process is dictated by diffusion or surface kinetics. The measurement protocol and the methodology for distinguishing the observed processes are described in detail in Note 2 of the ESI.† Variation in sweep rates allows determining the parameter b, which is then used to define the charge storage behavior according to eqn (S1).† HC-MPA/10BS hybrid material was chosen for these measurements owing to a more pronounced current response due to higher Bi_2S_3 loading. The measured CVs show the presence of all three reversible peaks at five selected sweep rates (Fig. 3a). During reduction, the peak at 390 mV shifts to slightly lower voltages with the increase of the sweep rate, while no difference is observed for the other two peaks. The parameter b values for the first two peaks (590 mV and 390 mV) during reduction are determined to be 0.713 and 0.715 (Fig. 3b), respectively. According to the literature,[43] the numbers suggest that the electrochemical reactions at these potentials are a combination of both surface and diffusion-driven processes ($0.5 \leq b \leq 1$). The b value for the 15 mV peak that appears due to the sodium intercalation into the HC (pores and graphene interlayer spaces[13,44,45]) is 0.495, implying that this particular process is diffusion-driven ($b \leq 0.5$). In the oxidation step, reverse reactions take place – the b value for the 120 mV peak (sodium deintercalation) is 0.335, indicating that diffusion is the limiting process at this potential. The b values for the 640 mV and 780 mV peaks are 0.783 and 0.811, respectively, implicating surface and diffusion-driven processes. The latter combination allows for faster electrochemical reactions in hybrid HC materials. It can be noted, that during reduction, the 15 mV diffusion-driven intercalation peak at higher sweep rates is not fully completed, as the curve abruptly stops at the lower cut-off voltage (Fig. 3a). Such an incomplete intercalation process might be caused by either sodium ions staying trapped in storage places or transport limitations. Further lowering of the cut-off voltage risks sodium plating at the HC surface (potentials below 0 V). During oxidation, the 120 mV peak shifts to higher voltages with an increased sweep rate, which indicates transport limitations during the deintercalation. For both reduction and oxidation, no voltage shifts can be observed for the other measured peaks (Fig. 3a). This implies that the Bi_2S_3 nanocrystals' surface and diffusion-driven transformation stay constant at different sweep rates and proceed faster than the sodium (de)intercalation.

An *operando* XRD measurement was performed to track and assign the structural changes in the hybrid HC materials involving the phase transformations of the Bi_2S_3 nanocrystals upon discharge (sodiation) and charge (desodiaton). The initial XRD pattern is consistent with the Bi_2S_3 reference phase (ICDD: 00-043-1471, the purple curve in Fig. 4). The first phase transformation is observed at 1.4 V, where the formation of a metallic bismuth phase (ICDD: 00-001-0688) occurs. At the onset of the first plateau at around 750 mV, the metallic bismuth phase starts to transform into a NaBi phase (ICDD: 03-065-2805) *via* the alloying process, reaching the complete phase transformation by the end of the plateau at 600 mV. The second plateau begins at 450 mV, initiating further sodiation of NaBi and resulting in the formation of Na_3Bi by the end of the plateau. No further phase transformations are observed until the end

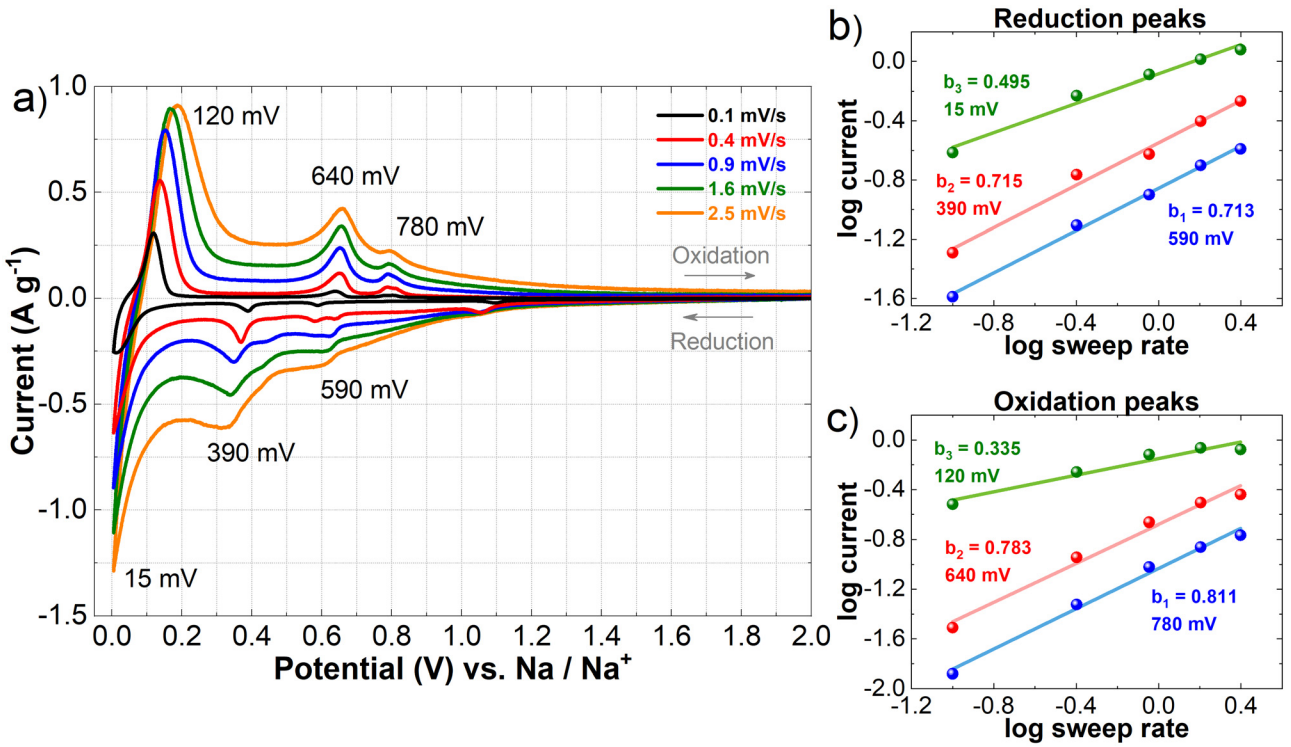

Fig. 3 Three-electrode cyclic voltammetry measurements of HC-MPA/10BS: (a) current responses at different scan rates, (b) determination of the parameter *b* for reduction peaks, and (c) determination of the parameter *b* for oxidation peaks.

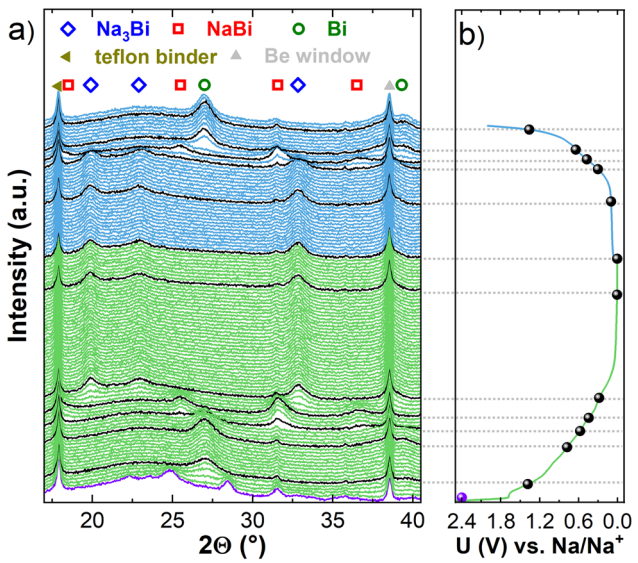

Fig. 4 *Operando* XRD measurements of HC-MPA/10BS. (a) *operando* XRD spectra and (b)the corresponding galvanostatic curve of the first cycle. Sodiation is designated with green color, while desodiation is designated with blue color. The black points on the right graph correspond to the diffractograms marked with black on the left graph.

of the sodiation step at around 5 mV. Here, at low potentials, sodium intercalation between the graphene layers as well as the filling of pores is taking place.[12,39] In the consequent desodiation step, no changes in the low voltage plateau are observed. The first observable difference appears in the sloping region at 300 mV, where the Na_3Bi phase transitions back to NaBi. With further desodiation, the NaBi phase transforms into the metallic bismuth phase. Combining *operando* XRD results with CV measurements, it can be concluded that the processes occurring in the high voltage region correspond to the electrochemical reaction of sodium with the Bi_2S_3 nanocrystals. More specifically, the formation of first-stage NaBi alloy at 590 mV is followed by further transformation to second-stage Na_3Bi alloy at 390 mV. Meanwhile, the processes in the low voltage region correspond to the sodium intercalation and pore filling in HC. A comparison of the contour plots of HC and HC-MPA/10BS can be found in ESI (Fig. S15).†

At the end of the desodiation step, the measured patterns do not resemble the Bi_2S_3 reference pattern. This indicates that Bi_2S_3 nanocrystals react irreversibly with sodium already in the initial cycle. While bismuth-containing compounds were detected and identified, *operando* XRD did not reveal any sulfur-containing crystalline structures. According to the literature, the formation of Na_2S and Na_2S_4 phases was observed during cycling.[34] For this reason, *ex situ* solid-state ^{23}Na MAS NMR measurements were employed at various depths of discharge (DoD). This enabled the differentiation of sulfur compounds and allowed assigning each of them to a specific DoD (Fig. 5a). Indeed, a broad peak is observed in all ^{23}Na MAS NMR spectra at approximately 50 ppm, corresponding to the formation of Na_2S (Fig. 5b). ^{23}Na nuclei have a relatively large

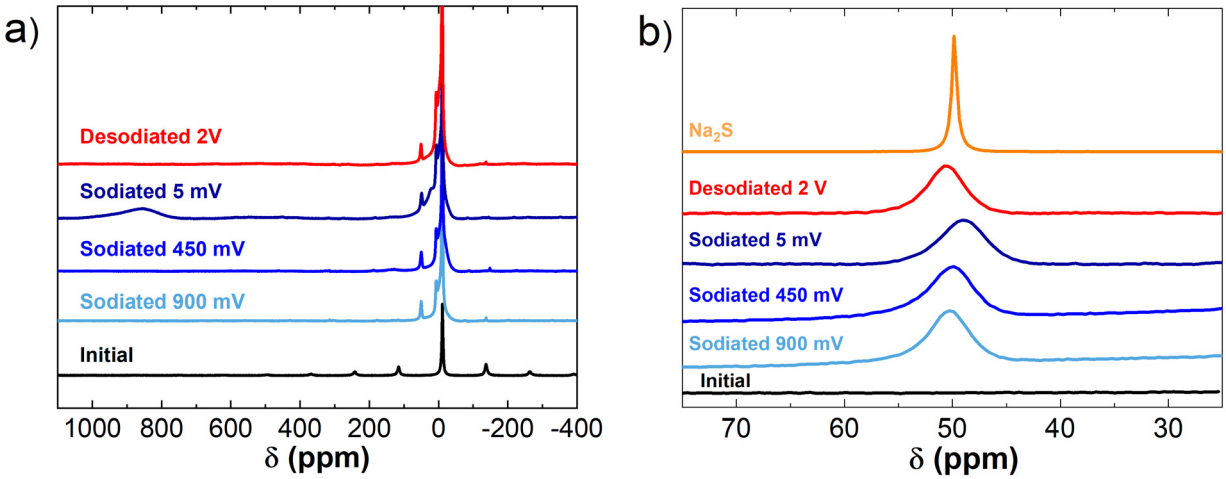

Fig. 5 *Ex situ* solid-state ^{23}Na MAS NMR spectra of HC-MPA/10BS powder extracted in the sodiated and desodiated state: (a) whole NMR spectra, and (b) inset corresponding to the positions ascribed to Na_2S. Initial material and Na_2S standard are added for reference.

quadrupolar moment, meaning that narrow symmetric ^{23}Na signals point to the sodium nuclei that either (i) occupy a very symmetric position such as in cubic symmetry, or (ii) are very mobile so that they see the anisotropic quadrupolar interaction being averaged out on the NMR time scale. All spectra demonstrate broader peaks compared to that of crystalline Na_2S, pointing to the more disordered structure of the formed compound.[46] This may be because in the hybrid HC-MPA/BS system Na_2S does not form large crystallites but stays in a more disordered formation. The presence of disorder inevitably leads to the smearing of the signals. The disorder of Na_2S structure makes it less visible by XRD, where crystallites below 5 nm in size are hard to detect. The position of the Na_2S peak also differs in the sodiated state at 5 mV. Here, it is positioned at 49.1 ppm, while in other spectra it is positioned at 50.8 ppm. The possible physical reason for the change in the isotropic shift is the anisotropic bulk magnetic susceptibility effect due to the conductivity change between the fully sodiated and desodiated state.[47] Additionally, a broad peak is observed at approximately 800 ppm (Fig. 5a) in the sodiated state (5 mV), corresponding to the sodium intercalated into the HC structure.[48] This peak is reversible during sodiation and desodiation. The fact that Na_2S is already detected in the sample sodiated to 900 mV indicates that upon the breakdown of the Bi_2S_3 structure sodium ions readily react with sulfur. This was observed as the CV current response peak at 1.1 V, which corresponds to the formation of Na_2S (Fig. S5c and d†).

High-resolution STEM imaging was conducted to study the changes in the morphology of HC hybrid material during cycling (Note 3 of ESI).† Fig. S6† shows STEM images of HC-MPA/10BS at lower magnification in the pristine (before cycling), sodiated (5th discharge), and desodiated (5th charge) state, providing a broader overview of the changes in the pristine material's morphology that occur upon cycling. In the case of the pristine material, the HC is tightly packed with Bi_2S_3 rod-like nanocrystals (Fig. S6a†). At higher magnifications (Fig. 6a), one can see that the Bi_2S_3 nanocrystals are highly crystalline, with sizes ranging ~30–50 nm in length and up to ~5–7 nm in width, and are interwoven into clearly distinguishable layered bundles of HC structure.

Upon sodiation (Fig. 6b and Fig. S6b†), nanocrystals change their shape significantly from nanorods to roundly shaped nanoparticles with sizes ranging from ~3 to ~20 nm. Some of the nanoparticles expose clear crystalline structure, while many appear to be amorphous (Fig. S6b†). Additionally, some bright smeared contrast can be seen in HAADF-STEM images in areas between nanoparticles, revealing either single heavier atoms or clusters of the latter spread all over the HC matrix. This additionally confirms the irreversible reaction of Bi_2S_3 nanocrystals with sodium upon cycling observed during *operando* XRD. Moreover, due to sodium intercalation, the HC structure becomes inflated, and its layered porous structure is not visible anymore. This observed phenomenon has a direct impact on the hybrid material's volume change upon sodiation. The quantity of sodium present in the material in the sodiated state amounts to 18 at% (Fig. S7†). The amount of bismuth is rather low at 0.2 at%, however, it can be seen that it is homogeneously distributed in the form of single atoms or nanoclusters at the surface of the HC. The low amount is most probably due to the increased amount of other elements, such as oxygen and sodium. Additionally, a high fluorine content is observed (6 at%), arising from the SEI formation on the HC surface due to the decomposition of the electrolyte salt ($NaPF_6$) and FEC additive. A similar picture is observed in the case of desodiated hybrid material (Fig. S6c† and Fig. 6c). Upon desodiation, no further changes in the shape of rounded nanocrystals can be observed. Although sodium is extracted from the HC at the end of desodiation, the HC structure keeps its disordered morphology and the graphene layers' bundles are hardly notable. The amount of sodium in the desodiated state is 14 at% (Fig. S8†), a minor decrease compared to the sodiated state. This suggests that sodium remains trapped in

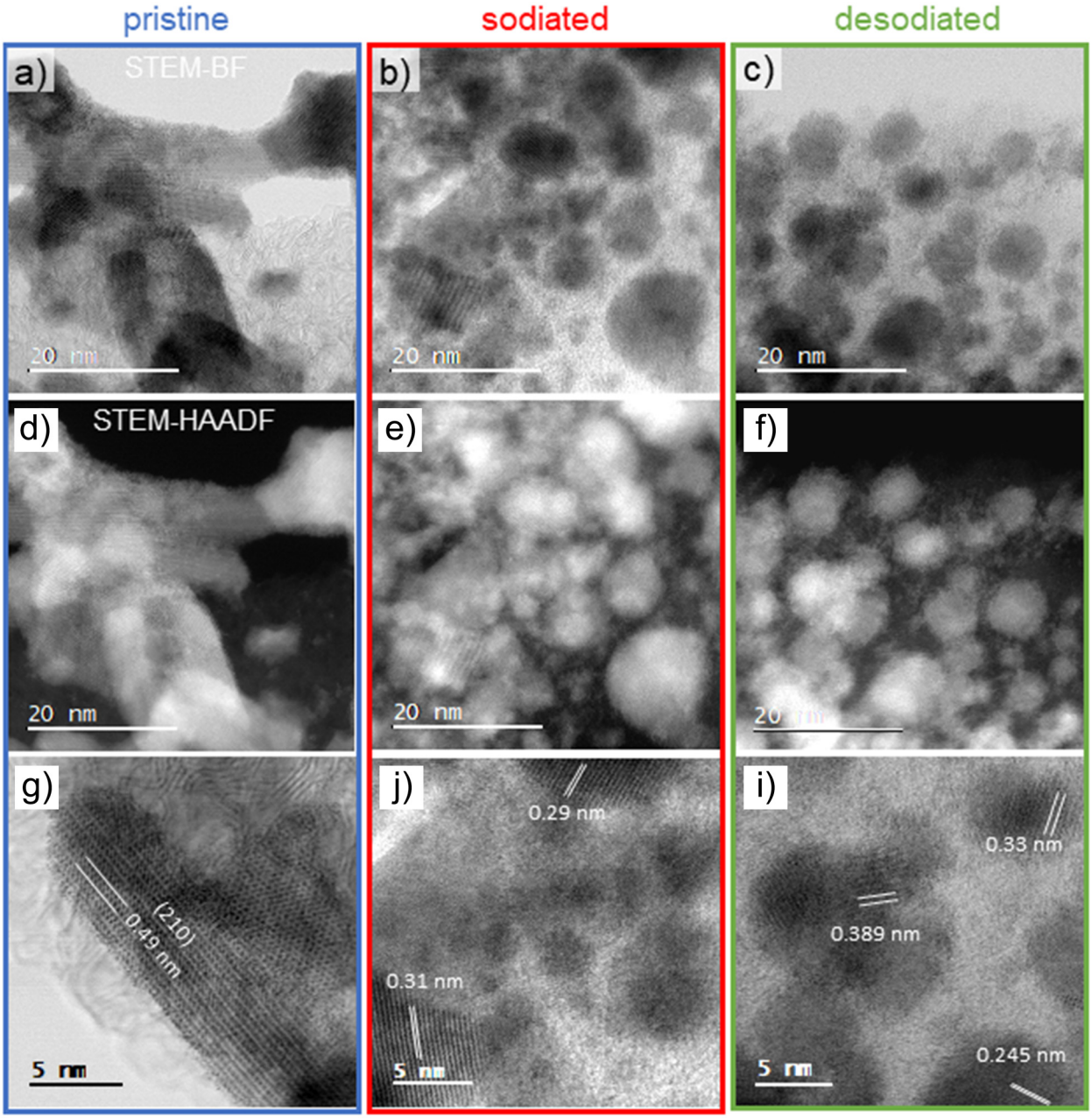

Fig. 6 STEM images of HC-MPA/10BS at higher magnifications, in (a), (d), (g) pristine, (b), (e), (h) sodiated and (c), (f), (i) desodiated state.

the hybrid material's structure even after desodiation. Furthermore, a certain amount of sodium residue stays in the form of organometallic compounds as SEI constituents. The amount of bismuth slightly increases to 0.8 at%, simultaneous with the decrease of sodium content. Sulfur content remains approximately the same in both states (0.4 at%).

In literature, the sodiation of Bi_2S_3 rods and the formation of sodiated structures were tracked at the atomic level. The crystal structures formed upon sodiation were deduced from the HRTEM images *via* FFT patterns.[49] However, from HR-STEM images of both sodiated and desodiated electrodes obtained in this study, the crystalline structure (measurable and marked distances between planes formed upon sodiation and desodiation in Fig. 6) could not be clarified *via* measurements of *d* spacings in FFT patterns. This is due to the FFT patterns' pixel size of 0.3 Å being much higher than the differences in *d* spacings of a large number of possible reflections in all structures observed during *operando* XRD during cycling, namely pristine Bi_2S_3, Bi-like metal, Na_2S, NaBI, and Na_3Bi (see Table S1† for example).

Considering the presented results, the following sodium charge storage mechanism in hybrid HC materials is depicted

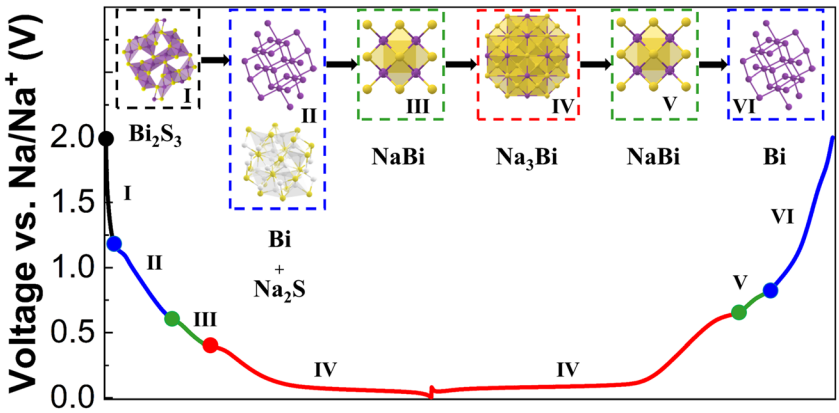

Fig. 7 Schematic representation of sodium charge storage mechanism in HC-MPA/BS.

in Fig. 7. During the discharge (sodiation), four distinct regions in the galvanostatic curve can be described *via* the following electrochemical reactions:

$$Bi_2S_3 + 6Na^+ + 6e^- \rightarrow 2Bi + 3Na_2S \quad \text{(Region I, II)}$$

$$Bi + Na^+ + e^- \leftrightarrow NaBi \quad \text{(Region III)}$$

$$NaBi + 2Na^+ + 2e^- \leftrightarrow Na_3Bi \quad \text{(Region IV)}$$

In Region I, the crystal structure of Bi_2S_3 breaks down into metallic bismuth and elemental sulfur during cell operation. The latter rapidly reacts with sodium in a conversion-type reaction in Region II forming Na_2S. Further, the metallic bismuth phase forms NaBi at lower potentials in Region III. Simultaneously in all three regions, the adsorption of sodium ions on carbon surface and defects takes place.[39] NaBi further transforms to Na_3Bi in Region IV. There, upon reaching the low voltage plateau, sodium ion intercalation between the graphene layers ensues, as was confirmed by *ex situ* solid-state ^{23}Na NMR (Fig. 5a).

During charge (desodiation) two distinct regions in the galvanostatic curve can be described *via* the following electrochemical reactions:

$$Na_3Bi \leftrightarrow NaBi + 2Na^+ + 2e^- \quad \text{(Region V)}$$

$$NaBi \leftrightarrow Bi + Na^+ + e^- \quad \text{(Region VI)}$$

In Region V, sodium ions deintercalation from the HC graphene layers occurs first, followed by dealloying of Na_3Bi to NaBi in Region VI. NaBi then subsequently transforms into a metallic bismuth phase. The desorption of sodium ions from the HC surface and defects occur concurrently. At the end of desodiation, the Bi_2S_3 structure is not restored.

3. Conclusion

In this study, the influence of the addition of layered bismuth chalcogenide nanorods to HC substrate material on the SIBs cycling performance was explored from morphological, structural, atomic, and electrochemical points of view. The hybrid HC/BS and HC-MPA/BS negative electrode materials were synthesized using plain or MPA-modified HC as a substrate for 5 wt% and 10 wt% loadings of Bi_2S_3 nanoparticles in nanorods morphology. To the best of our knowledge, such an HC hybridization approach has not yet been reported, especially with the use of bonding-promoting linkers.

XPS measurements demonstrated that the addition of MPA leads to more stable bonding Bi_2S_3 nanoparticles to the HC surface, which results in better electrochemical performance. The overall capacity boost for the hybrid HC-MPA/BS systems was achieved with 5 wt% Bi_2S_3 nanoparticles mass loading (increase from 216 mA h g^{-1} for HC to 252 mA h g^{-1} for HC-MPA/5BS after 100 cycles), while 10 wt% Bi_2S_3 nanoparticles mass loading had an inferior cycling performance compared to that of pure HC material. However, the CV behavior for both loadings was similar, which implied analogous charge storage mechanisms. The three-electrode measurements at different sweep rates showed that the combination of diffusion and surface-driven reactions due to the presence of Bi_2S_3 could be observed in the high voltage region, while the processes in the low voltage region, corresponding to sodium intercalation into the HC matrix, exhibited a strictly diffusive behavior. Detailed insight into the structural transformations of HC-MPA/BS hybrid material upon electrochemical cycling was gained *via operando* XRD measurements. These have elucidated the irreversible nature of Bi_2S_3 transformation upon interaction with sodium due to the formation of Na_2S. Based on these observations, we have proposed a sodium charge storage mechanism for the HC-MPA/BS hybrid system: (i) upon cycling, simultaneous reactions of sodium with Bi_2S_3 nanorods as well as with the HC occur; (ii) reversible alloying reactions can be achieved even at high current densities resulting in the formation of intermediate NaBi and final Na_3Bi phases; (iii) the conversion reactions result in the irreversible formation of the Na_2S phase. It is reasonable to speculate, that the higher amount of formed Na_2S in the hybrid HC material with 10 wt% of Bi_2S_3 is the reason for its electrochemical performance inferior to that of 5 wt% of Bi_2S_3.

4. Experimental section

Materials

Hard carbons were obtained by a two-step pyrolysis of corncob, as reported in our previous work.[41] The final pyrolysis temperature was selected at 1400 °C. After the pyrolysis, the obtained hard carbon was ground in a mixer mill (SPEX SamplePrep, Retsch) for 10 min.

Synthesis of Bi_2S_3 nanocrystals was performed following the hot-injection method reported by Bernechea *et al.*,[32] using bismuth acetate and hexamethyldisilathiane as precursors and oleic acid as solvent and capping ligand. Obtained Bi_2S_3 nanocrystals were finally dispersed and stored in toluene.

Hybrid HC/Bi_2S_3 materials were prepared by mixing the HC powder with the solution containing Bi_2S_3 nanocrystals (1.4 g L^{-1} in toluene) for 20 minutes under constant magnetic stirring. The obtained product was washed with toluene several times to remove any residual nanocrystals and subsequently dried at 80 °C. Carbon functionalization with the MPA linker was performed by mixing the hard carbon powder with a 1 M MPA, 0.1 M H_2SO_4 solution in acetonitrile for 30 minutes, then washing the samples with acetonitrile, and drying at 80 °C. After MPA functionalization, Bi_2S_3 nanocrystals were added following the aforementioned protocol.

The obtained materials were denoted as HC, HC/BS, and HC-MPA/BS for the non-modified carbon, carbon with the addition of Bi_2S_3 nanocrystals and carbon with the MPA-based substrate as well as Bi_2S_3 nanocrystals, respectively.

Characterization

The crystal structure of the samples was characterized *via* X-ray powder diffraction (XRD). Measurements were carried out on a PANalytical X'pert PRO high-resolution diffractometer with Cu $K\alpha_1$ radiation (λ = 1.5406 Å) in the range of 2θ from 10° to 80° with a step of 0.033° and a measurement time of 1 s per step.

Thermogravimetric analysis (TGA) was performed under airflow (50 mL min^{-1}), in a temperature range between 35 °C and 1000 °C at a heating rate of 10 °C min^{-1} on a METTLER Toledo equipment.

X-ray photoelectron spectroscopy (XPS) was performed with an Axis Supra spectrometer (Kratos Tech). The spectra were excited by a monochromatized Al Kα source at 1486.6 eV. Analysis of the peaks was performed with the CasaXPS software and the binding energies were referenced to the internal C 1s standard at 284.6 eV.

Scanning electron microscope (SEM) images and Energy-dispersive X-ray spectroscopy (EDX) analysis were performed in an SEM Inspect 50.

The changes in Bi_2S_3 nanocrystal morphology and particles' distribution over a range of sodiation and desodiation steps were examined in a JEM-ARM200CF, probe C_s-corrected scanning transmission electron microscope (STEM), equipped with a cold field emission (FEG) electron source operated at 80 kV, a JEOL Centurio 100 mm^2 EDXS detector and JEOL STEM detectors (JEOL, Tokyo, Japan). For the materials imaging, scanning high-resolution high-angle annular dark-field/bright-field (STEM-HAADF, STEM-BF) modes were used. Additional information is presented in Note 3 of ESI.†

Phase transformations taking place during cycling were characterized by *operando* XRD measurements on a Bruker D8 high-resolution diffractometer using Cu $K\alpha_1$ radiation (λ = 1.5406 Å). Electrochemical measurements were carried out within a potential window between 2 V and 0.005 V *vs.* Na/Na^+ with a current of 10 mA g^{-1}, which corresponds to C/30 current density. Only the initial sodiation and desodiation steps were performed. Additional information is presented in Note 4 of ESI.†

Solid-state magic angle spinning (MAS) nuclear magnetic resonance (NMR) spectra were recorded on a 600 MHz VNMRS spectrometer (Agilent Technologies) using a 1.6 mm Triple Resonance HXY FastMAS Varian Probe. The shift axis in all the spectra was referenced using an external, secondary reference of adamantane (the ^{13}C signal of the CH_2 groups was set to 38.3 ppm). We can consider the reported shifts to be accurate to within ±0.2 ppm. Larmor frequencies of ^{23}Na nuclei were 158.539 MHz and sample MAS frequencies were 20 kHz for the measurements. ^{23}Na spectra were recorded using an excitation pulse with a duration of 1.0 μs, 20 000 scans, and a 0.1 s delay between scans. For the needs of *ex situ* NMR measurements, the same protocol was employed as described in Note 3 of ESI.† The only difference in the preparation of the *ex situ* sample was that the powder was not washed before the transfer to the NMR probe.

Electrode preparation, cell assembly, and electrochemical measurements

Electrodes were prepared with a composition of 90 wt% of active material (HC or HC/BS or HC-MPA/BS), 5 wt% conductive carbon Super C65 (Timcal) and 5 wt% polyvinylidene fluoride (PVdF, Aldrich), unless stated otherwise. The mixture was dissolved in *N*-methyl pyrrolidone (NMP, Aldrich) and ball milled for 30 min at 300 rpm to obtain a homogeneous slurry. The slurry was then cast on a carbon-coated Al foil (Armor, France) with a doctor blade applicator of a thickness of 100 μm. The coated slurry was dried at 80 °C overnight. Electrodes with a diameter of 15 mm were punched out the next day and transferred to an argon-filled glovebox. The loadings were maintained between 1.5 and 2 mg cm^{-2}.

The prolonged cycling measurements were conducted in two-electrode 2032-type coin cells. The cells were assembled in an argon-filled glovebox with water and oxygen contents below 0.5 ppm. HC, HC/BS, or HC-MPA/BS electrodes were used as working electrodes whereas sodium metal (Aldrich) was used as the counter electrode. Both electrodes were separated by a glass fiber separator (Whatman GF-A). The electrolyte used was 1 M $NaPF_6$ in a solvent mixture of ethylene carbonate (EC) and dimethyl carbonate (DMC) (1 : 1 vol%) with the addition of 2 wt% of fluoroethylene carbonate (FEC). Each cell was filled with 100 μL of the electrolyte. Electrochemical measurements were carried out within a potential window between 2 V and 0.005 V *vs.* Na/Na^+ employing the following protocol: 5 formation cycles with the current of 30 mA g^{-1} (theoretical

capacity was taken according to the model proposed by Bommier,[13] *i.e.* 301.6 mA h g^{-1}), which roughly translates to a rate of C/10. After the formation cycles, the current switched to a higher rate of 300 mA g^{-1} (corresponding to a rate of 1C) and was measured for another 100 cycles. At the end of each discharge, a constant voltage step was applied at the lower cut-off, limited to 5 h or until the current rate was lower than C/100.

Rate performance measurements were carried out within a potential window between 2 V and 0.005 V *vs.* Na/Na^+ employing the following protocol: 3 formation cycles with the current of 30 mA g^{-1} (C/10) with applied constant voltage at the lower cut-off. Afterwards, the currents of 60 mA g^{-1} (C/5), 150 mA g^{-1} (C/2), 300 mA g^{-1} (1C), 600 mA g^{-1} (2C), and 1500 mA g^{-1} (5C) were applied with 5 cycles performed at each current. Finally, the current was decreased back to 30 mA g^{-1} (C/10) and 10 more cycles were performed.

Three-electrode cells (Hohsen Corp., Japan) were assembled for cyclic voltammetry measurements. HC or HC-MPA/BS electrodes were used as the working electrode while two separate sodium metal electrodes were prepared to implement as the counter and reference electrode. The three-electrode cell setup is presented in Fig. S4.† The current response was measured at different scan rates, ranging from 2 V to 0.005 V. Pseudocapacitive and diffusion-limited processes occurring during reduction and oxidation were distinguished by the current response through the power-law relationship. Additional information is presented in Note 2 of ESI.†

Conflicts of interest

There are no conflicts to declare

Acknowledgements

This research received financial support from the European Union's Horizon 2020 research and innovation program under grant agreement no. 875629 (NAIMA) and M-ERA.NET network: Slovenian Ministry of education, science and sport with NOEL project, and MCIN/AEI/10.13039/501100011033 (Ref. PCI2019-103637). We further acknowledge financial support from the Slovenian Research Agency (research core funding P2-0423, and research project N2-0266), CERIC-ERIC Consortium, CIBER-BBN, ICTS "NANBIOSIS", ICTS ELECMI node "Laboratorio de Microscopias Avanzadas", and Servicio General de Apoyo a la Investigación-SAI, Universidad de Zaragoza. Additionally, B. T., R. D, and A. V. acknowledge the research support by the NATO Science for Peace and Security (SPS) Programme under grant G5836-SUPERCAR.

References

1 H. Ritchie and M. Roser, Energy Production and Consumption, **https://ourworldindata.org/energy-production-consumption**, (accessed 13 April 2022).
2 D. Kundu, E. Talaie, V. Duffort and L. F. Nazar, *Angew. Chem., Int. Ed.*, 2015, **54**, 3432–3448.
3 C. Vaalma, D. Buchholz, M. Weil and S. Passerini, *Nat. Rev. Mater.*, 2018, **3**, 18013.
4 H. Moriwake, A. Kuwabara, C. A. J. Fisher and Y. Ikuhara, *RSC Adv.*, 2017, **7**, 36550–36554.
5 X. Dou, I. Hasa, D. Saurel, C. Vaalma, L. Wu, D. Buchholz, D. Bresser, S. Komaba and S. Passerini, *Mater. Today*, 2019, **23**, 87–104.
6 M. Thompson, Q. Xia, Z. Hu and X. S. Zhao, *Mater. Adv.*, 2021, **2**, 5881–5905.
7 C. Matei Ghimbeu, A. Beda, B. Réty, H. El Marouazi, A. Vizintin, B. Tratnik, L. Simonin, J. Michel, J. Abou-Rjeily and R. Dominko, *Adv. Energy Mater.*, 2024, 2303833.
8 L. Simonin, C. Saavedra Rios, A. de Geyer, C. Matei Ghimbeu and C. Dupont, *Energies*, 2020, **13**(14), 3513.
9 C. Nita, B. Zhang, J. Dentzer and C. Matei Ghimbeu, *J. Energy Chem.*, 2021, **58**, 207–218.
10 M. Dahbi, M. Kiso, K. Kubota, T. Horiba, T. Chafik, K. Hida, T. Matsuyama and S. Komaba, *J. Mater. Chem. A*, 2017, **5**, 9917–9928.
11 A. Beda, C. Vaulot, F. Rabuel, M. Morcrette and C. Matei Ghimbeu, *Energy Adv.*, 2022, **1**, 185–190.
12 T. Zhang, J. Mao, X. Liu, M. Xuan, K. Bi, X. L. Zhang, J. Hu, J. Fan, S. Chen and G. Shao, *RSC Adv.*, 2017, **7**, 41504–41511.
13 C. Bommier, T. W. Surta, M. Dolgos and X. Ji, *Nano Lett.*, 2015, **15**, 5888–5892.
14 S. Alvin, C. Chandra and J. Kim, *Chem. Eng. J.*, 2020, **391**, 123576.
15 W. Li, M. Zhou, H. Li, K. Wang, S. Cheng and K. Jiang, *Energy Environ. Sci.*, 2015, **8**, 2916–2921.
16 K. Schutjajew, J. Pampel, W. Zhang, M. Antonietti and M. Oschatz, *Small*, 2021, **17**, 2006767.
17 T. J. Bandosz and T.-Z. Ren, *Carbon*, 2017, **118**, 561–577.
18 D. Zhou and L. Z. Fan, *Ionics*, 2018, **24**, 3065–3073.
19 M. Dirican, Y. Lu, Y. Ge, O. Yildiz and X. Zhang, *ACS Appl. Mater. Interfaces*, 2015, **7**, 18387–18396.
20 X. Zhao, C. Yan, X. Gu, L. Li, P. Dai, D. Li and H. Zhang, *ChemElectroChem*, 2017, **4**, 1516–1522.
21 W. Li, S. Hu, X. Luo, Z. Li, X. Sun, M. Li, F. Liu and Y. Yu, *Adv. Mater.*, 2017, **29**, 1605820.
22 X. Shi, S. Chen, H. Fan, X. Chen, D. Yuan, Q. Tang, A. Hu, W. Luo and H. Liu, *ChemSusChem*, 2019, **12**, 4046–4053.
23 H. Tao, M. Zhou, K. Wang, S. Cheng and K. Jiang, *J. Alloys Compd.*, 2018, **754**, 199–206.
24 C. Yan, X. Gu, L. Zhang, Y. Wang, L. Yan, D. Liu, L. Li, P. Dai and X. Zhao, *J. Mater. Chem. A*, 2018, **6**, 17371–17377.
25 W. Ren, H. Zhang, C. Guan and C. Cheng, *Adv. Funct. Mater.*, 2021, **17**(48), 2006767.
26 M. Wang, Q. Wang, X. Ding, Y. Wang, Y. Xin, P. Singh, F. Wu and H. Gao, *Interdiscip. Mater.*, 2022, **1**, 373–395.
27 S. Dai, L. Wang, M. Cao, Z. Zhong, Y. Shen and M. Wang, *Mater. Today Energy*, 2019, **12**, 114–128.

28 D. Wang, C. Hao, W. Zheng, X. Ma, D. Chu, Q. Peng and Y. Li, *Nano Res.*, 2009, **2**, 130–134.
29 X. Sun, L. Wang, C. Li, D. Wang, I. Sikandar, R. Man, F. Tian, Y. Qian and L. Xu, *Nano Res.*, 2021, **14**, 4696–4703.
30 Z. Dang, W. Meng, D. Zuo, D. Li, L. Jiang and D. Fang, *Electrochim. Acta*, 2022, **425**, 140752.
31 C. Lu, Z. Li, L. Yu, L. Zhang, Z. Xia, T. Jiang, W. Yin, S. Dou, Z. Liu and J. Sun, *Nano Res.*, 2018, **11**, 4614–4626.
32 M. Bernechea, Y. Cao and G. Konstantatos, *J. Mater. Chem. A*, 2015, **3**, 20642–20648.
33 J. Ni, X. Bi, Y. Jiang, L. Li and J. Lu, *Nano Energy*, 2017, **34**, 356–366.
34 W. Sun, X. Rui, D. Zhang, Y. Jiang, Z. Sun, H. Liu and S. Dou, *J. Power Sources*, 2016, **309**, 135–140.
35 W.-J. Li, C. Han, S.-L. Chou, J.-Z. Wang, Z. Li, Y.-M. Kang, H.-K. Liu and S.-X. Dou, *Chem. – Eur. J.*, 2016, **22**, 590–597.
36 J. Sottmann, R. Homs-Regojo, D. S. Wragg, H. Fjellvåg, S. Margadonna and H. Emerich, *J. Appl. Crystallogr.*, 2016, **49**, 1972–1981.
37 W. Yang, H. Wang, T. Liu and L. Gao, *Mater. Lett.*, 2016, **167**, 102–105.
38 Z. Zhang, C. Zhou, L. Huang, X. Wang, Y. Qu, Y. Lai and J. Li, *Electrochim. Acta*, 2013, **114**, 88–94.
39 C. Wang, J. Lu, H. Tong, S. Wu, D. Wang, B. Liu, L. Cheng, Z. Lin, L. Hu, H. Wang, W. Zhang and Q. Chen, *Nano Res.*, 2021, **14**, 3545–3551.
40 T. K. Patil, *Pelagia Research Library Advances in Applied Science Research*, 2013, **4**, 115–122.
41 B. Tratnik, N. Van de Velde, I. Jerman, G. Kapun, E. Tchernychova, M. Tomšič, A. Jamnik, B. Genorio, A. Vizintin and R. Dominko, *ACS Appl. Energy Mater.*, 2022, **5**, 10667–10679.
42 H. Yuan, F. Ma, X. Wei, S. Jia, P. Kang, Y. Yu, X. Yang and J.-L. Lan, *Mater. Today Energy*, 2022, **28**, 101084.
43 H. Lindström, S. Södergren, A. Solbrand, H. Rensmo, J. Hjelm, A. Hagfeldt and S.-E. Lindquist, *J. Phys. Chem. B*, 1997, **101**, 7717–7722.
44 Y. Morikawa, S. Nishimura, R. Hashimoto, M. Ohnuma and A. Yamada, *Adv. Energy Mater.*, 2020, **10**, 1903176.
45 Z. V. Bobyleva, O. A. Drozhzhin, K. A. Dosaev, A. Kamiyama, S. V. Ryazantsev, S. Komaba and E. V. Antipov, *Electrochim. Acta*, 2020, **354**, 136647.
46 G. Mali, M. U. M. Patel, M. Mazaj and R. Dominko, *Chem. – Eur. J.*, 2016, **22**, 3355–3360.
47 R. Pigliapochi, L. O'Brien, A. J. Pell, M. W. Gaultois, Y. Janssen, P. G. Khalifah and C. P. Grey, *J. Am. Chem. Soc.*, 2019, **141**, 13089–13100.
48 J. M. Stratford, P. K. Allan, O. Pecher, P. A. Chater and C. P. Grey, *Chem. Commun.*, 2016, **52**, 12430–12433.
49 R. Cai, W. Zhang, J. Zhou, K. Yang, L. Sun, L. Yang, L. Ran, R. Shao, T. Fukuda, G. Tan, H. Liu, J. Wan, Q. Zhang and L. Dong, *Small Methods*, 2022, **6**, 2200995.